Two-dimensional viscous froth model for foam dynamics

N. Kern,[1,2] D. Weaire,[1] A. Martin,[1] S. Hutzler,[1] and S. J. Cox[1]

[1]*Physics Department, Trinity College, Dublin 2, Ireland*
[2]*Laboratoire des Verres, Université Montpellier II, Montpellier, France*

The two-dimensional viscous froth model is a simple tractable model for foam rheology and coarsening. It includes, but is not confined to, the quasistatic regime. Here we present a detailed analysis and implementation of the model, illustrated with various examples. With certain simplifying assumptions, it provides significant insight into strain-rate-dependent effects in foam rheology and elsewhere, particularly in relation to recent experiments.

I. INTRODUCTION

A simple model for a viscous froth was first introduced over one decade ago, in the context of domain growth [1,2]. Its full potential is still to emerge, as the model is adapted and applied to foam rheology. It can provide a natural approach to the analysis of the quasi-two-dimensional (2D) scenarios which currently receive a great deal of experimental attention [3,4]. We offer a thorough discussion of the model, and its various limiting cases. We then present results obtained using numerical implementations of the model. We first address the dynamics of isolated topological events in a foam (the relaxation following film rupture and topological change), before examining the effect of viscous drag in a simple rheological situation (trains of bubbles passing through a bend in a channel).

The viscous froth model was initially conceived as a generalization of two existing paradigms for coarsening dynamics of cellular patterns, the ideal *soap froth* and ideal *grain growth* models. Indeed, it has the appealing feature of bridging between these two cases, which are found when appropriate limits are taken. It is analytically tractable in many respects, because of the simple form taken for viscous drag. This may not be an accurate representation of any particular experimental realization of a 2D froth, but it should still be a good qualitative guide in most cases. Its relevance to the 3D case is less clear, and indeed the very mechanisms of dissipation in that case remain obscure [5]. Nevertheless, past experience suggests that the 2D viscous froth model is an important step towards developing our understanding of 3D foam dynamics.

A related method of simulation has been used by Cantat and Delannay [4] for the interpretation of experiments on two-dimensional rheology and flow. This approach, due originally to Fullman [6] and to Kawasaki [7,8], replaces the interfaces with straight lines and concentrates the viscous dissipation at the vertices. It is sometimes characterized by the term "vertex model." The result is a tractable model for computation, which should capture most of the main effects, but does not proceed by controlled approximation.

Here we wish to focus on local events in the flow, for which full geometrical details are essential. The model that we describe here incorporates both the cell pressures and the curvatures of the soap films. We expect that systematic stud-

ies with varying degrees of geometrical refinement will eventually allow us to reliably assess the accuracy of Kawasaki-type dynamics over a range of flow velocities.

Our intention is to provide a model that is appropriate for the case of foams with low liquid fraction. The opposite limit, the dynamics of foams with high liquid content, has been addressed by the "bubble mechanics model" of Durian [9].

II. THE 2D VISCOUS FROTH MODEL

We have in mind a cluster of N cells or bubbles $\{b\}$, each containing gas at a certain pressure P_b. The interfaces separating the bubbles are subject to a (constant) interfacial tension γ. This describes a static two-dimensional foam of negligible liquid fraction, a so-called *dry* foam.

The viscous froth model adds dynamics to this description. Inertia is not included, being negligible in typical real 2D foam systems. The equation of motion is then given by the following equilibrium of forces acting locally at each point on a soap film, in the direction of the normal, as illustrated in Fig. 1:

$$\Delta P_{bb'}(s) - \gamma K_{bb'}(s) = \lambda v(s). \tag{1}$$

Here s represents the position on the film shared by bubbles b and b'. The individual terms are the forces (per unit length) acting on a segment of the interface. $\Delta P_{bb'}$ is the pressure difference between the bubbles and $K_{bb'}$ is the curvature of
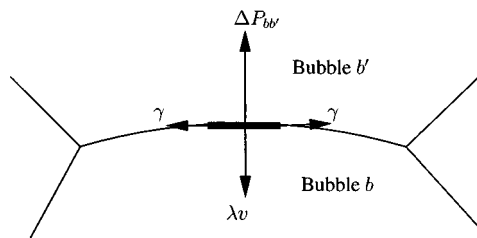

FIG. 1. The forces acting on a segment of soap film of length l are due to surface tension γ, the pressure difference between neighboring bubbles $\Delta P_{bb'}$, and a dissipative force per unit length λv proportional to the film velocity. In the case illustrated, the film moves upward.

70 041411-1

TABLE I. Notation and notes for dimensional analysis. We refer to a two-dimensional geometry, in which pressure is defined as force per unit length and surface tension has the dimension of a force.

Quantity	Symbol	
pressure	P	force/length
surface tension	γ	force
curvature	K	$1/$length
drag coefficient	λ	force $\times$ time/length^2
permeability	κ	length$^2/($force $\times$ time$)$

the interface. The right-hand side represents a local dissipative force opposing the motion of the interface, with a drag coefficient λ, the origin of which depends on the experimental situation under consideration. v is the normal velocity of the interface; only normal velocities are considered, since they are sufficient to describe the temporal evolution of the structure. Such a model, incorporating only normal forces of the simple form described, does appear to offer a satisfactory qualitative account of experiments [10]. However, it may well need elaboration in the future to incorporate such additional effects as that of the longitudinal motion of liquid in the Plateau borders.

Each relevant quantity in a two-dimensional geometry is given in Table I, with a note of its relation to force, length, and time, for the purposes of dimensional analysis. The structure may be subject to change, for example due to coarsening (diffusion of gas between bubbles) or imposed shear. Both these processes have associated time scales, relating to diffusion rate and shear rate, respectively. The comparison between each of these and the time scale of the structural relaxation is crucial, as it determines whether the foam may be regarded as being effectively in equilibrium. Most analyses of coarsening and rheology have relied on the assumption that this is so. It is our intention to go beyond this *quasistatic* approximation.

A. Limiting cases

We first isolate the three limiting cases of the viscous froth model as it is given in Eq. (1), which are illustrated in Fig. 2.

1. Ideal soap froth

This is the simplified case in which the drag is negligible, i.e., the velocities are small in the sense that $\lambda v \ll \gamma K \simeq \Delta P$. In the limiting case, Eq. (1) then simply reduces to the Laplace law

$$\Delta P_{bb'} = \gamma K_{bb'}(s). \qquad (2)$$

In this commonly applied approximation, the effect of diffusion or shear is treated as a slowly varying (quasistatic) constraint and the structure evolves through a sequence of equilibrium states, which correspond to minima of the interfacial energy. This evolution is continuous except at topological changes, as described in Sec. II D. Each equilibrium struc-
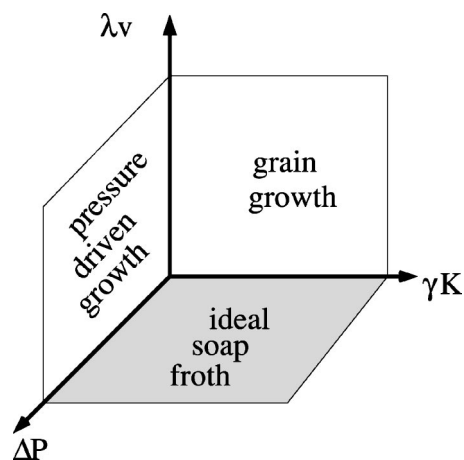

FIG. 2. Limiting cases of the viscous froth model. In the regions close to the three planes shown, the force balance on a film segment is achieved by compensation of two dominating terms, the third being negligible. In these limit cases, simpler models are recovered.

ture obeys Plateau's rules (see, e.g., [11]), which we recall for the two-dimensional case: films are arcs of circles which meet in threes at the vertices, where they intersect at angles of 120 degrees. In addition, curvatures must add to zero at every vertex, for consistency with the Laplace law for cell pressure differences [Eq. (2)].

Subtleties arise from topological changes, such as that which is provoked when an interface between two bubbles shrinks to a point. This would then lead to a fourfold vertex, which is known to immediately dissociate into two threefold vertices [11], thus effectively performing a neighbor swapping of bubbles (T1). In the soap froth model, this would occur instantaneously, thereby leading to infinite velocities. We shall return later to the effect of dissipation on the dynamics of such events.

The original interest in the ideal soap froth model, which uses the quasistatic approximation, was focused on the dynamics of the *coarsening* that occurs when the interfaces are permeable to the gas present in the bubbles. The permeability constant κ is defined via Fick's law as

$$\frac{dA_b}{dt} = \kappa \sum_{b'} \Delta P_{bb'} l_{bb'}, \qquad (3)$$

where A_b is the area of bubble b. The constant κ consequently has units of volume per energy and time, like an inverse viscosity. As time evolves, the bubble areas follow Von Neumann's law [12],

$$\frac{dA_b}{dt} = \frac{\pi}{3} \kappa \gamma \, (n_b - 6), \qquad (4)$$

where n_b is the number of sides of bubble b. In the quasistatic regime considered here, the Von Neumann law follows simply from Eqs. (2) and (3) and the 120-degree condition for vertices [11].

2. Grain growth

Another limiting case is attained when pressure differences between bubbles are negligible: $\Delta P_{bb'} \ll \gamma K \simeq \lambda v$. The motion of boundaries is then driven by curvature, as described below. Originally, this model arose in the context of domain growth in metals [13], for which there are no relevant cell pressures. The interface motion in this limiting case is local curvature-driven growth,

$$v(s) = -\frac{\gamma}{\lambda} K(s). \tag{5}$$

Although the overdamped dynamics described by Eq. (5) allows for arbitrary shapes of the interface, angles of 120 degrees at vertices are maintained, except instantaneously at topological changes [14], as described below.

The motion of the interface results in some bubbles growing at the expense of others, leading to coarsening dynamics that obey a law of the same type as the soap froth,

$$\frac{dA_b}{dt} = \frac{\pi}{3}\frac{\gamma}{\lambda}(n_b - 6). \tag{6}$$

This is known as Mullin's law for grain growth [13]. It is, at first sight, remarkable that two apparently different models have this important relation, as expressed in Eq. (4) and (6), in common.

3. Pressure-driven growth

Finally, surface tension forces may not contribute significantly: $\gamma K \ll \lambda v \simeq \Delta P$, and in this case we are dealing with interface motion directly driven by a pressure difference. Then, the normal motion is uniform on each film. This does not seem to be a situation that arises in typical rheological experiments, and we shall not pursue it further.

B. Two-dimensional rheology

The development of rheological devices in a quasi-two-dimensional geometry has been the focus of much activity over the past few years. In one type of experiment, a foam is confined between two parallel plates [3,15]. When their separation is small compared to the size of individual bubbles, this constitutes an approximate realization of a two-dimensional dry foam, provided the liquid content is kept small [16]. Such devices allow convenient imaging of the foam structure as the foam flows, or as it is subjected to external perturbations such as shear of the boundaries. For example, a simple shear ζ may be imposed on boundaries, at a shear rate $\dot{\zeta}$, as sketched in Fig. 3.

The quasistatic model of soap froth has been applied by several groups to describe the rheology of a dry foam [3,17–20]. It provides a straightforward description in the limiting case where deformation is sufficiently slow that viscous effects remain negligible, i.e., in the limit where the time scale of relaxation after a topological change (bubble rearrangement) is much less than that associated with the shear rate. Strictly speaking, even in this limiting case the model has an important shortcoming related to topological
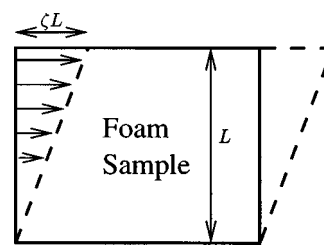

FIG. 3. A sketch of a 2D simple shear experiment on a foam sample of width L. The shear is denoted ζ, with a shear rate $\dot{\zeta}$. We characterize this with the time scale T_ζ.

changes: if combinations (avalanches) of topological changes occur, the order in which they are triggered is arbitrary and depends upon the algorithm used. This arbitrariness in the quasistatic model has been recognized from the outset [17,18,20], but has not been resolved.

The viscous froth model provides at least a tentative description of realistic dynamics, in which the drag coefficient λ represents the effect of viscous dissipation in the Plateau borders as they slide along the glass plates. The underlying dissipation relation linking the drag force to a given velocity is nontrivial, and known to involve rather subtle hydrodynamics [21]. These suggest a power law relating the drag force and the normal velocity,

$$f_{\text{drag}} = -\lambda v^\nu, \tag{7}$$

and the predicted exponent ($\nu = 2/3$) has indeed been measured for simple quasi-2D foam structures confined between two parallel glass plates [10].

For the purpose of the present paper, we shall adhere to the simplifying choice of a linear drag relation ($\nu = 1$), as in the original viscous froth model. It is conceptually straightforward to generalize to the nonlinear case, but we shall show below that the choice of linearity allows for significant simplifications in the analysis and numerical implementation. We expect this more transparent model to retain the essential qualitative behavior following from any more realistic dissipation relation, which includes values of ν different from unity.

C. Time scales

The parameters entering the basic viscous froth model are the tension in the films γ, and their associated drag coefficient λ. A simple dimensional analysis reveals the scaling behavior of the model.

1. Relaxation dynamics

We introduce a length scale R characteristic of the structure, such as the mean bubble radius. In the absence of gas diffusion and an imposed shear, the only intrinsic time scale is set by γ, R and the drag coefficient λ as

$$T_\lambda = \frac{\lambda R^2}{\gamma}. \tag{8}$$

In Sec. III, we will describe the results of a numerical implementation of the viscous froth model, allowing us to

relate specific relaxation times to T_λ. In particular, it gives the characteristic time associated with relaxation after a topological change. The topological change itself, which changes the connectivity, is instantaneous in the present model. An interesting case is presented in the experiments of Monnereau *et al.* [22], where the time *between* topological changes is of the same order as the relaxation time. We will return to this case in future work.

2. Coarsening dynamics

In its original spirit, the viscous froth model was formulated to interpolate between the coarsening behavior of soap froth and grain growth models [1,2]. The presence of diffusion sets an additional time scale through the permeability constant κ, as

$$T_\kappa = \frac{R^2}{\kappa \gamma}. \tag{9}$$

The associated coarsening dynamics has been shown [2] to obey

$$\frac{dA_b}{dt} = \frac{\pi}{3} \frac{\kappa \gamma}{1 + \lambda \kappa} (n_b - 6). \tag{10}$$

This is in the form of a generalized Von Neumann law with an appropriately redefined prefactor. The dimensionless ratio of the two time scales,

$$\frac{T_\lambda}{T_\kappa} = \lambda \kappa, \tag{11}$$

is indeed seen to be the relevant parameter which interpolates between the limiting cases of the original Von Neumann law [Eq. (3)] for a coarsening soap froth ($T_\lambda \ll T_\kappa$) and Mullins' law [Eq. (6)] for grain growth ($T_\lambda \gg T_\kappa$). These limits can be illustrated in a schematic diagram, Fig. 4, providing a comprehensive picture of the viscous froth model for coarsening, which it is interesting to highlight before introducing rheology.

3. Rheology (shear)

In many rheological experiments, gas diffusion is negligible on the time scale of the experiment, and hence the bubble areas do not vary as a function of time. In this case, the relevant time scale is defined through the shear rate $\dot{\zeta}$,

$$T_\zeta = 1/\dot{\zeta}. \tag{12}$$

The ratio of the intrinsic time scale (set by the viscous drag) to the imposed one (set by the shear rate) is then given by

$$\frac{T_\lambda}{T_\zeta} = \frac{\lambda R^2 \dot{\zeta}}{\gamma}. \tag{13}$$

For quasistatic shear, this ratio is much less than 1. It is the only nondimensional parameter when diffusion is negligible
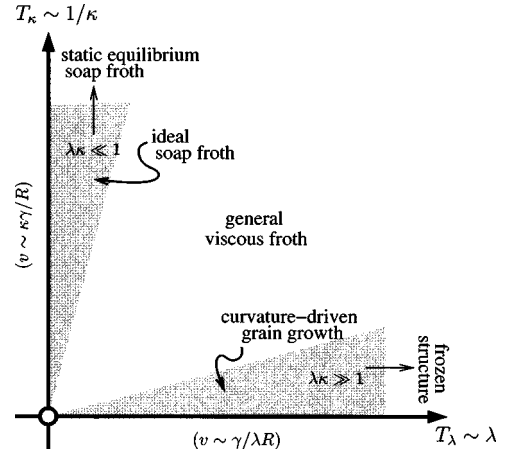

FIG. 4. Illustration of limiting cases within the viscous froth model for coarsening dynamics in terms of the time scales associated with the drag coefficient λ and the diffusion constant κ. As the relaxation time associated with the drag, T_λ, becomes infinite, the structure becomes frozen, while infinite T_κ corresponds to no coarsening and a static equilibrium soap froth. The conventional soap froth and grain growth models arise in the shaded regions and their associated axes. Also indicated on the axes are the velocities arising during coarsening.

($T_\kappa \gg T_\lambda, T_\zeta$), the case upon which we shall focus. However, diffusion could be included very easily in the implementation presented below, thus accommodating all three time scales in the model.

D. Vertex dynamics

To what rules does the motion of a vertex conform in the present model? This question was raised in the context of curvature-driven growth [1,2]. It is not immediately evident that the motion of the boundaries according to curvature entails any simple local rule, but this is the case [23]. In Appendix A, we briefly reconsider this problem, in order to generalize the previous results to the viscous froth model, and add some discussion of singular cases. Our most important conclusion in the present context is that the viscous froth model should retain angles of 120 degrees between films at a vertex, as in the two limiting cases of grain growth and the ideal soap froth.

Despite this general conclusion, appropriate to a dry froth, angles not equal to 120 degrees can still arise instantaneously in various ways. First, one might choose an initial configuration with such anomalous angles. Even if this is the case, the angles must conform to the 120 degrees rule at all later times until a topological change is encountered. We show in Appendix A that this implies an *infinite* initial velocity for the vertex. Secondly, something similar happens whenever a T1 change is made, upon the formation of a fourfold vertex (or indeed more complex topological changes). We address the consequences of these conclusions by means of a numerical representation of the viscous froth model [Eq. (1)], which we now introduce.
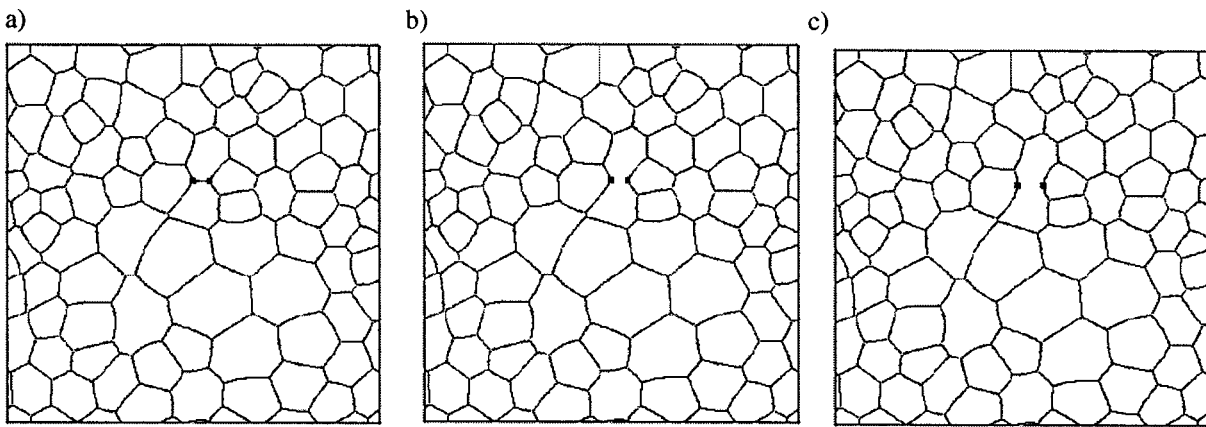
FIG. 5. (a) Example of a relaxed periodic structure with 83 cells and total area equal to one. (b) The film between the two marked vertices is removed and the structure is allowed to relax under the viscous froth rules of motion. (c) The final equilibrium structure.

E. Numerical implementation

We have implemented the viscous froth dynamics numerically, using a discretized representation of the network of films, as in the earlier work of, for example, Frost and Thompson [24]. The details are given in Appendix B. Rather than considering the general case of an arbitrary exponent ν in the dissipation law [Eq. (7)], we focus on the special case of a linear dissipation relation ($\nu=1$), as in the original viscous froth model. The general case is easily treatable but the linear case allows for a more efficient numerical scheme for determining the bubble pressures while it should also provide a reasonable description of realistic dynamics.

The outline of our implementation is as follows. At each time step, we perform geometric calculations to determine surface tension forces at each point. The motion of the cell edges also depends on the cell pressures which act upon them. Any particular choice for the cell pressures will result in corresponding changes in the cell areas, the relationship being linear. But the changes in cell areas are independently determined by the generalized von Neumann law [Eq. (10)], and hence are known. (In particular, they are *zero* when the permeability is zero.) Hence the pressures are uniquely determined by invoking consistency with Eq. (10). The existence of the generalized von Neumann law thus reduces to a single solution of linear equations a problem that would otherwise require a more obscure iterative process. The details of this calculation are given in Appendix B. Having thus established the forces acting on each element of film, we then find the velocity of each point of the discretization from Eq. (1) and update the shape of the films accordingly.

In addition to coding these simulations *ab initio*, we have developed an alternative treatment, based on the Surface Evolver [25]. This version facilitates dealing with finite foams in constrained geometries such as those described in Sec. III C. It relies upon the Surface Evolver for all the necessary topological "bookkeeping" and adherence to boundaries (e.g., solid walls), while it equally implements the numerical scheme described in Appendix B, expressed in the Evolver's command language.

In the following, we shall retreat to nondimensional quantities, as appropriate for numerical study. They can easily be transformed into the relevant dimensional quantities, as described in Appendix B, using the length scale R (representing the mean bubble radius as before) and the resulting energy scale γR and (2D) pressure scale γ/R.

III. SIMULATION OF THE DYNAMICS OF ISOLATED TOPOLOGICAL EVENTS

Our ultimate aim is to study the response of a bubble cluster to external or internal perturbations. On the scale of the entire foam, this relates to its rheology. As a first step, however, it is necessary to characterize the simpler processes on a local level, which ultimately determine the flow behavior on a larger scale. Here we shall focus on the two most important examples, the relaxation which follows the rupture of a film and the topological change entailed by a neighbor swapping event. These are the singular cases of initial conditions to which reference was made earlier.

In the limiting case of curvature-driven growth, Brakke [14] has analyzed the dynamics of these processes, among others, with mathematical rigor. Here we are interested in the effect of dissipation in the framework of the viscous froth model.
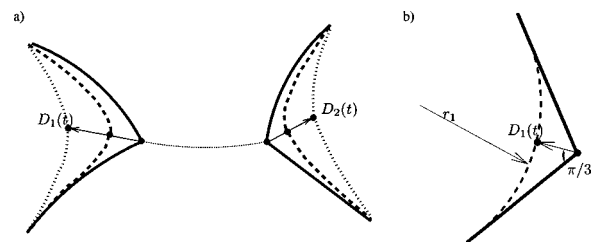

FIG. 6. (a) A sketch of the change in topology due to an induced film rupture. Solid lines show the initial state. Dashed lines show different configurations during the relaxation of the structure after the rupture. We measure $D(t)=D_1(t)+D_2(t)$ over time, which shows an initial square-root behavior before an exponential relaxation to equilibrium. (b) In the early stages of the film rupture, the remaining films can be approximated by arcs of radius r_1 traversing an area a_1 from their initial position. This allows us to construct upper and lower bounds to the value of the constant Δ_0 describing the evolution.
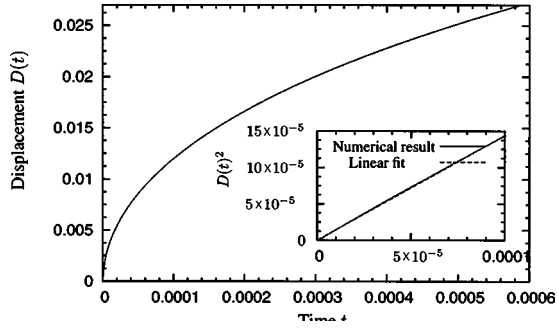
FIG. 7. The increases in the square of the distance of the vertices from their original position, $D(t)$, after film rupture. The length scale R is set by the mean bubble area, $\langle A \rangle = \frac{1}{83}$. Time is measured in units of $T_\lambda = \lambda R^2 / \gamma$, and the time step was $\delta t = 10^{-6}$. For the short times shown in the inset, the data follow a square-root power law with coefficient $\Delta_0 \approx 1.18$.

A. Film rupture

The first step is to produce an equilibrated foam structure, in order to provide a well-defined starting point. This is done by setting up a foam structure and using viscous froth dynamics to thoroughly relax the system until energy and cell areas have converged. An example of such a structure is shown in Fig. 5(a).

One film is then chosen and ruptured, i.e., deleted from the structure, thus coalescing two bubbles into one. The resulting bubble has two "kinks." We are interested in how the structure relaxes away from this singular configuration. We therefore measure the straight-line distance $D_i(t)$ which a kink has moved away from its initial position, as illustrated in Fig. 6(a).

Figure 5 shows an example of such a film rupture simulation. We distinguish the initial regime of singular dynamics immediately following the coalescence, localized around the topological change, from a long-term exponential relaxation of the foam structure to equilibrium (see Sec. III B). Note that the final equilibrium configuration shown here remains strained, corresponding to only a local energy minimum; the system would relax further if T1s were initiated on the resulting short edges, but these do not occur naturally in such a dry foam.

The displacement grows in a singular way from time $t=0$, corresponding to a relaxation of the kinks with an infinite initial velocity. The data in this initial behavior well described by a power law,

$$D(t) = D_1(t) + D_2(t) = \Delta_0 \sqrt{t}. \tag{14}$$

The constant Δ_0 is determined by fitting D^2 to a polynomial function, shown in Fig. 7. The results for four rupture events on the 83-bubble foam illustrated give an estimated value of $\Delta_0 = 1.18 \pm 0.02$. We note in passing that this initial square-root regime may be traced back to the behavior of the grain growth model, for which it is well known [14]: choosing an (arbitrarily) small area around the kink, it follows from the argument used in Appendix A that pressure forces cannot affect the initial dynamics.

A lower bound to the value of Δ_0 in Eq. (14) can thus be obtained as follows. We consider the short-time regime in which the pressures are insignificant and the films adjacent to the ruptured one develop a large (initially infinite) curvature $1/r_1$—see Fig. 6(b). Therefore, the velocity of the original vertex is given by $dD_1/dt = 1/r_1$ and geometry gives $D_1(t) = r_1(2/\sqrt{3}-1)$. Eliminating r_1 and solving gives $D_1(t) = k\sqrt{t}$ with $k = \sqrt{2(2/\sqrt{3}-1)} \approx 0.556$. Since we overestimate the curvature in this way, this provides a lower bound to the velocity, and therefore a lower bound to Δ_0 is $\Delta_0^{\text{low}} = D(t)/\sqrt{t} = 2k \approx 1.11$, in close agreement with the value $\Delta_0 = 1.18$ obtained in the simulations.

In a similar manner, by calculating the area a_1 swept out by the film, we can calculate an upper bound to Δ_0. Von Neumann's law states that $da_1/dt = \pi/3$, while geometrical considerations show that $a_1 = r_1^2(1/\sqrt{3} - \pi/6)$. Using the relationship between $D_1(t)$ and r_1 given above, we find an upper bound

$$\Delta_0^{\text{up}} = \frac{D(t)}{\sqrt{t}} = 2\sqrt{\frac{\pi(1/\sqrt{3} - \pi/6)}{3(2/\sqrt{3} - 1)^2}} \approx 1.36. \tag{15}$$

Note that in practice both these arguments can be extended to provide bounds for the case of any included angle rather than just $2\pi/3$.

B. Neighbor swapping (T1)

Another aspect of great importance to the temporal evolution of a foam structure is the dynamics of a single T1 topological change, involving a neighbor switch between four bubbles—see Fig. 8. To create a single T1, we choose one film and slowly vary the volumes of the four neighboring bubbles, in such a way as to obtain a thoroughly equilibrated structure with the chosen edge length close to zero. After updating the topology according to the T1 topological
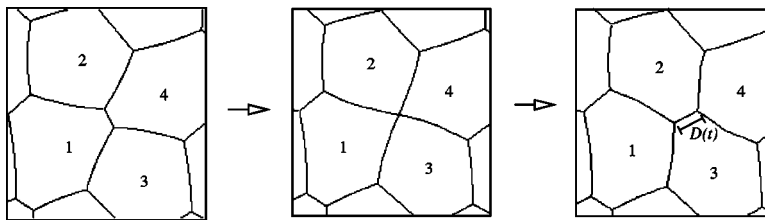

FIG. 8. Sketch of neighbor swapping event. We inflate and deflate bubbles as required to create a zero-length film. The topology is then changed according to a T1 neighbor swapping process, and the system is allowed to evolve following viscous froth dynamics. We measure the increase in length of the new film, $D(t)$.
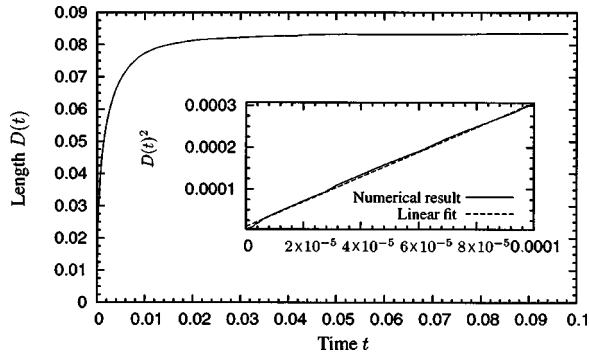
FIG. 9. The increase in the length of the new film, $D(t)$, after a T1 event. The length is measured in units of R associated with the mean bubble area $\langle A \rangle = \frac{1}{83}$ and time is in units of $T_\lambda = \lambda R^2 / \gamma$. The time step was $\delta t = 10^{-6}$. The inset shows the square of the length, which is a straight line (with a small offset due to the vertex separation at the T1, which is finite but very small) since the data follow a square-root power law with coefficient $\Delta_1 \approx 1.7$.

change, we let the system evolve and measure the increase in length of the new film, denoted $D(t)$ (see Fig. 9). Again, there is an initial square-root increase,

$$D(t) = \Delta_1 \sqrt{t}. \qquad (16)$$

For long times, as the structure approaches a new equilibrium, the motion of the network slows down exponentially. An example is shown in Fig. 10. In this regime, the length D is no longer a good measure of the structural response. Instead, we evaluate the overall edge length

$$l_{\text{tot}}(t) = l_\infty + \Delta_\infty e^{-t/\tau_\infty}, \qquad (17)$$

where l_∞ is the edge length of the relaxed structure.

In this case we performed four simulations. We estimate $\Delta_\infty \approx 1.3$ and $\tau_\infty \approx 0.02 = 1.66 T_\lambda$ for the asymptotic time constant.

C. Application to neighbor switching in a bent channel

As a further illustration of the implementation of the model, we will present results for an ordered 2D foam struc-
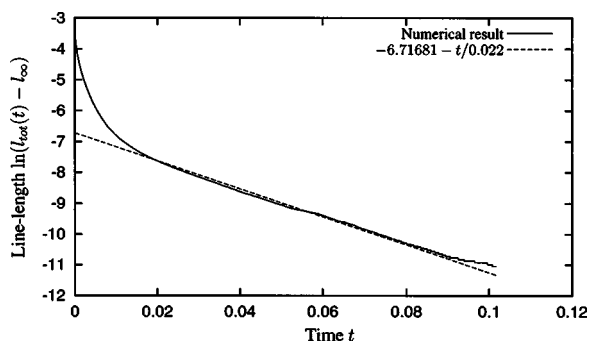

FIG. 10. Example of the long-time dynamics after a T1 topological change, for the same simulation as in Fig. 9, during which the structure relaxes exponentially to a new equilibrium. The total length of all films is plotted over time, to give a relaxation time in Eq. (17) of $\tau_\infty \approx 0.02$.
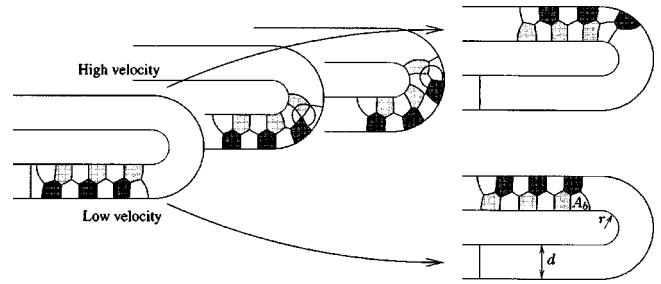

FIG. 11. Viscous froth simulations of a 2D ordered foam structure flowing around a 180° bend of width d and radius of curvature r. The initial configuration is shown on the left. At low velocity (in this case $v = 0.8$), there is no topological change and the final structure is indistinguishable from that of a quasistatic calculation. At a higher velocity (e.g., $v = 1.1$), the bubbles successively change neighbors due to a T1 transformation (circled) as they pass close to the apex of the bend. As the velocity is increased, the T1 position moves farther around the channel, away from the start.

ture which is forced through a narrow channel with a 180° bend, as in Fig. 11. This is one of many interesting experimental devices demonstrated in the experiments of Weaire *et al.* [26]; further details will be given in Drenckhan [27]. In this case, a chain of pairs of bubbles is pushed through the channel; if the rate at which this moves is sufficiently great, then a T1 topological change occurs somewhere in the bend, causing bubbles that were originally neighbors to move apart. A quasistatic simulation of this experiment does *not* show the neighbor switching, in keeping with the low-velocity experimental results. This problem thus provides a very appropriate qualitative test of the viscous froth model.

For this purpose, it is practical to use the Surface Evolver version of our code, mostly in order to accommodate the constraints representing the sides of the channel. The values of the geometric constants defining the shape of the channel are clearly important design parameters for such a device, and we will explore their effect on the dynamics in future work. For the present, we vary only the bubble area and bubble velocity to demonstrate the application of the viscous froth model.

In the simulations described here, the channel is of width $d = 2$ and the bend has an inner radius of curvature $r = 1$, shown in Fig. 11. We insert a chain of 12 bubbles in pairs, all with the same area A_b. We introduce a single bubble of area A_0 at one end of the channel whose area we inflate at a rate $\dot{A}_0$ in order to push the other bubbles around the bend. The bubbles therefore move at a velocity $v = \dot{A}_0/d$.

The only other significant parameter is a cutoff length l_c: a film between two vertices which is shorter than l_c is deleted, allowing a T1 to occur. The parameter l_c is related to the liquid fraction—with higher values, the T1 changes can occur when two vertices are further apart, as in a wetter foam. We fix this to be $l_c = 0.01$; this corresponds to a rather dry foam, but again, its influence will be investigated in future work.

Rather than a shear ζ of the whole sample, discussed above, this introduces a more complicated deformation which may be characterized by the time scale
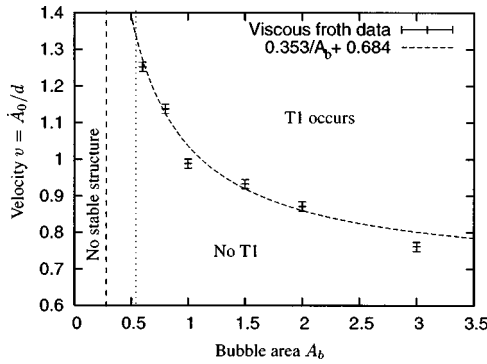
FIG. 12. The ordered foam structure is pushed around the bend in Fig. 11 with velocity v. At a sufficiently large value of the velocity, a topological T1 change occurs. This critical value of velocity v_c is shown—it decreases in inverse proportion to the bubble size (the line is $v=0.353/A_b+0.684$), within the limits of possible structures. Outside these limits, i.e., for small values of bubble area less than about $A_b=0.28$ and larger values greater than about $A_b=4$, it is not possible to create a stable structure of this type in the channel. For bubble areas of between $A_b=0.28$ and 0.6, a rather different behavior occurs at high velocity in which the T1 is seen only for alternate bubble pairs (see Fig. 13).

$$T_b = \frac{r^2}{\dot{A}_0}. \tag{18}$$

That is, the outer films move a distance πd greater than the inner films, over a distance πr. The shear therefore varies by an amount d/r over a time $\pi r/v$, giving a shear rate $v\, d/r^2$ which leads to the above time scale. T_b is roughly equivalent to T_ζ.

We find, as expected, that for low velocities (i.e., close to the quasistatic limit) there is no topological change as the foam structure flows around the channel. The structure becomes more deformed as the velocity is increased, with a consequent reduction in the length of the inner films when they pass around the bend. At a critical value of velocity v_c, for given bubble area A_b, the length of one of these films shrinks to zero as it passes around the bend and the T1 occurs. The critical value of v_c for a range of bubble sizes is shown in Fig. 12: as the bubble size increases, this critical velocity decreases.

It seems clear that this critical velocity is determined by the competition between the two time scales T_λ and T_b, whose ratio T_λ/T_b is proportional to the product $A_b v$. If no other length scales are required to determine the time scale T_λ in this situation, the critical velocity should decrease with the bubble size. The line $v_c=0.353/A_b+0.684$ is shown in Fig. 12, and is in reasonable agreement with the numerical results.

In the simulations described here, there can be significant *end effects* associated with the front and back ends of the finite bubble train. These may also occur in the corresponding experiments, and we thus describe them in order to give a suggestion of the predictive power of the viscous froth model. First, note that we have considered only one possible orientation of the ordered foam structure—another possibil-
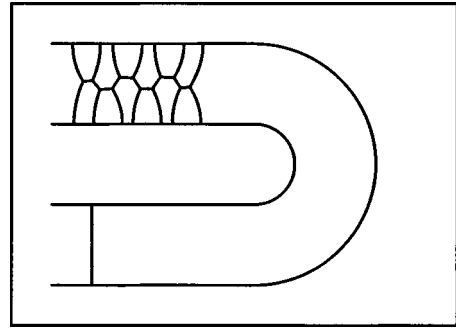

FIG. 13. For small bubbles, in this case $A_b=0.5$, a T1 transformation occurs only for alternate bubbles, leading to the final structure shown.

ity is for the leading (unshaded) bubble in Fig. 11 to be on the inside of the channel. In this case, the critical velocities are approximately a factor of 2 higher. Secondly, the leading and trailing bubbles do not behave in the same manner as those in the bulk of the foam structure, but if a T1 occurs for the leading bubble then the topological change will propagate through the structure.

For small bubble areas, it is not possible to make a stable ordered structure of the type shown in Fig. 11—instead the structure will be one in which three or more bubbles span the channel. Or, for slightly larger areas, a structure such as that shown in Fig. 13 can occur, with a T1 transformation only for alternate bubble pairs. For large bubble areas, the structure dissociates into a "bamboo" structure with plane parallel films separating bubbles that span the width of the channel.

The fact that such an elementary example has such a rich variety of behavior underlines the need for a simple method of simulation, if devices are to be designed to manipulate ordered foam structures [28].

IV. CONCLUSIONS

The two-dimensional viscous froth model provides a simple and tractable description of the dynamics of a foam by retaining viscous drag forces on the moving Plateau borders. We have revisited selected features of the model and discussed limiting cases as well as the general scaling features. A straightforward scheme has allowed us to implement a simulation of 2D viscous froth dynamics which retains full geometrical details. The simple form chosen for the viscous drag provides a good qualitative guide to the results of rheological experiments.

The present model is intended partly as a heuristic guide to the understanding of the effects of incorporating viscosity. As such, it should take a place alongside others [8,9] which have complementary advantages. Comparison with experiment, as presented here and in further work to be published, suggests that it can serve as a semiquantitative guide to the interpretation and design of specific experiments. In certain cases, we can observe deviations from the predictions of the model, such as apparent departures of vertex angles from 120 degrees, and we expect to develop refinements to cope with these. However, there are several different possible sources

TABLE II. A summary of some regimes of the 2D viscous froth model. The general case (all time scales of the same order) might be described as rheology and diffusion with dissipative effects.

$T_\lambda \ll T_\kappa, T_\zeta$	Ideal soap froth
	Quasistatic equilibrium description of general rheology with diffusion
	Instantaneous structural changes after topological rearrangements
$T_\lambda \ll T_\kappa \ll T_\zeta$	Ideal soap froth model applied to diffusion without rheology
	Von Neumann's law
$T_\lambda \ll T_\zeta \ll T_\kappa$	Ideal soap froth model applied to rheology without diffusion
$0 \ll T_\kappa \ll T_\zeta, T_\lambda$	Ideal grain growth (curvature driven)
	Mullins' law
$0 \ll T_\lambda, T_\zeta \ll T_\kappa$	**Viscous froth model applied to rheology without diffusion**
	Finite relaxation-time structural changes
	Fixed cell areas
$0 \ll T_\lambda, T_\kappa \ll T_\zeta$	**Viscous froth model applied to diffusion without rheology**
	Finite relaxation-time structural changes
	(*Generalized* Von Neumann law)
$0 \ll T_\lambda \ll T_\kappa, T_\zeta$	**Viscous relaxation to static equilibrium structure**

for such deviations, such as the changes in tension due to the stretching of the films [29], and most of them are not easily captured. There is also, for example, the possibility of a significant role for longitudinal flow in the Plateau borders. Systematic experiments will be undertaken to guide further progress in theory and simulation.

The first results from this model begin to shed light on the effect of the various competing time scales in the evolution of the froth, summarized in Table II. Application to a simple rheological situation has allowed us to show that the model qualitatively reproduces what has been observed in experimental work in a quasi-two-dimensional geometry. We anticipate application to further rheological experiments, with the requirement of a more detailed quantitative comparison. In particular, the model should prove a valuable tool for the efficient design of experiments and devices.

APPENDIX A: VERTEX DYNAMICS

To what rules does the motion of a vertex conform in the present model? This question was raised in the context of curvature-driven growth [1,2]. It is not immediately evident that the motion of the boundaries according to curvature entails any simple local rule, but this is the case. Here we shall generalize some previous results [1,2,23] to the viscous froth model to account for the role of cell pressures, and add some discussion of singular cases. To do so, we express the motion of a vertex as a translation (with velocity **v**) and a rotation (with angular velocity ω).

Vertex angles

Evolving structures in both the quasistatic soap froth and the grain growth models maintain angles of 120 degrees between films at a vertex. This remains valid for viscous froth dynamics.

To justify this, consider a small volume around a vertex, as illustrated in Fig. 14. The vertex is subject to the forces exerted by the film tensions, gas pressures, and drag forces. As the control volume shrinks to a point, only contributions from the tensions remain, and therefore a force balance between tensions alone must hold. The vertex itself remains in equilibrium and Plateau's rules imply angles of 120 degrees, as long as no explicit drag force on the vertices themselves is introduced. Frost and Thompson [24] have performed simulations in which all of the drag forces are located at the vertices. Here we will maintain the alternative assumption, that drag forces are exerted on the moving boundaries of the cells. The case of instantaneous configurations after topological changes, which may not respect the condition of 120 degree angles, will be discussed below.

Curvature sum rule

The velocity **v** of a vertex is required to be consistent with the motion of all three boundaries, if they are to continue to meet at a point. Each (normal) velocity is given by

$$\lambda \mathbf{v} \cdot \hat{\mathbf{n}}_i = \Delta P_i - \gamma K_i, \tag{A1}$$

where $i = 1, 2, 3$ labels the films joining a given vertex. The symmetry of the vertex dictates that
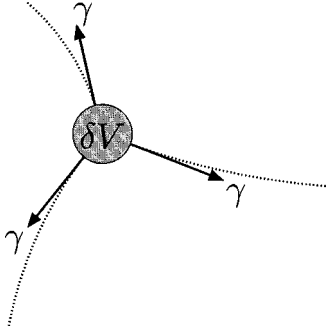
FIG. 14. Illustration of the force equilibrium on a control volume δV around a vertex, in the limit as $\delta V \rightarrow 0$. Both pressure forces and viscous forces vanish in this limit.

$$\sum_i \hat{\mathbf{n}}_i = 0. \qquad (A2)$$

Using this, as well as the fact that $\Sigma \Delta P_i = 0$, since the pressure differences are defined cyclically, the summation of Eq. (A1) for $i = 1, 2, 3$ gives

$$\sum_i K_i = 0, \qquad (A3)$$

where K_i stands for the limiting value of the film curvature as the vertex is approached. Hence it follows that the curvatures just around a vertex must add to zero, just as in the simpler curvature-driven case. Equation (A3) is a necessary condition, which holds at all times other than those of the instantaneous singular cases mentioned above.

Vertex translation

A general rule may be derived for the translation velocity **v** of a vertex, relating it to the curvatures of all three boundaries at the vertex. To obtain an explicit formula for **v**, we use

$$\mathbf{v} = \frac{2}{3} \sum_i \hat{\mathbf{n}}_i (\hat{\mathbf{n}}_i \cdot \mathbf{v}), \qquad (A4)$$

which again follows from vertex symmetry, in order to obtain

$$\lambda \mathbf{v} = \frac{2}{3} \sum_i (\Delta P_i - \gamma K_i) \hat{\mathbf{n}}_i. \qquad (A5)$$

This generalizes the previously derived rule [23] to incorporate pressure differences between bubbles.

For coarsening dynamics, we have shown that the quasistatic regime is characterized by $\lambda \kappa \ll 1$. Von Neumann's law [Eq. (4)] shows that the vertex velocities in this limit are of order $v_{\lambda \rightarrow 0} \sim \kappa \gamma / R$, where R is a measure of a cell size, e.g., its mean radius. Thus

$$\Delta P_i - \gamma K_i \sim \lambda \kappa \frac{\gamma}{R} \quad (\lambda \rightarrow 0) \qquad (A6)$$

in the more general viscous froth case. In the quasistatic limit, all velocities disappear asymptotically and no motion

takes place, except from singular shapes such as those to be discussed now.

Vertex rotation

We will omit the details of the derivation of the explicit formula for the rotational velocity ω of the vertex, which are contained in [23], and simply state the result,

$$\omega = \frac{1}{3} \frac{\gamma}{\lambda} \sum_i \frac{\partial K_i}{\partial s_i}. \qquad (A7)$$

Incidentally, it should be noted that the individual terms of the sum do *not* give the angular velocity of the corresponding arms of the vertex. Rather, there is an additional term, which evaluates to zero when all three expressions are averaged. The equality of rotational velocity of all three arms imposes further consistency conditions on **v**, K_i, and K_i', which will not be explored here.

Singular cases

The above argument applies to any vertex respecting the 120 degree condition. It is possible, however, to prepare a system in an initial configuration which does not respect these rules. In fact, topological changes naturally lead to such deviations in vertex angles (T1 process) or to kinks in the boundaries (film rupture). Since neither pressure forces nor drag forces act on a point, the surface tension force remains unbalanced, implying an infinite velocity. Such dynamics are illustrated in Sec. III.

In contrast, suppose now that the angular conditions are satisfied, but that the curvature sum rule $\Sigma K_i = 0$ is not. It is possible to define such an initial configuration. Just as an infinite velocity is entailed (only) at the vertex in the previous case, so an infinite angular velocity follows here. We may redefine curvatures precisely at the vertex, to satisfy $\Sigma K_i = 0$, but this entails an infinite term $\partial K_i / \partial s_i$ in each case: hence the infinite angular velocity, according to Eq. (A7).

APPENDIX B: NUMERICAL IMPLEMENTATION

We describe here the details of the numerical implementation of the viscous froth model. This is based upon a discretized representation of the network of films—refer to Fig. 15 for an illustration.

Dimensionless units

As indicated in the text, we first write the defining equations in terms of dimensionless variables: the typical energy scale is γR, and the (2D) pressure scale is γ / R, where R is, as before, the mean bubble radius. Thus we write Eq. (1) as

$$\Delta \tilde{p} - \tilde{K} = \tilde{v}, \qquad (B1)$$

where the dimensionless variables are

$$\tilde{p} = \frac{p}{\gamma / R}, \quad \tilde{K} = KR, \quad \text{and} \quad \tilde{v} = \frac{v}{\gamma / (\lambda R)}. \qquad (B2)$$

The model therefore contains no explicit parameters beyond the obvious scaling relations and, potentially, additional geo-
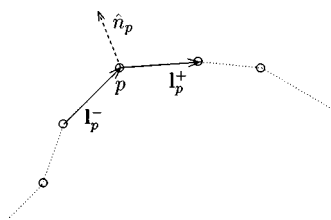
FIG. 15. Illustration of the discretized representation of the curve representing a film.

metrical properties of the structure (such as its polydispersity). Any externally imposed constraints, or additional features of the model, such as gas diffusion, will of course also introduce additional dimensionless parameters, as discussed in the main text.

Discretization

We have to resolve all films into a sequence of points, connected by line segments of finite length (edges). As the number of discretization points is increased, this can represent a smooth curve as closely as required. We denote the edge vectors associated with the segments by $\mathbf{l}_i$. All errors are dependent upon the average length of the discretized films, $\langle \mathbf{l}_i \rangle / R$, and the dispersity in edge length.

The pressure force associated with a point, which must also act in the normal direction, is therefore

$$\mathbf{F}_p^P = \Delta P l_p \hat{\mathbf{n}}_p, \tag{B3}$$

where we attribute one-half of each adjacent edge to a point p,

$$\mathbf{l}_p = \frac{1}{2}(\mathbf{l}_p^+ + \mathbf{l}_p^-). \tag{B4}$$

To make contact with the equation of motion [Eq. (1)], it may be useful to observe that this amounts to attributing a curvature vector

$$\mathbf{K} = \frac{\hat{\mathbf{l}}_p^+ - \hat{\mathbf{l}}_p^-}{|\mathbf{l}_p|} \approx \frac{\partial \hat{\mathbf{l}}}{\partial s} \tag{B5}$$

to each point p, as is indeed the lowest-order approximation to the definition of curvature intrinsic to the curve, as indicated in the last term of Eq. (B5). It would ultimately be desirable to incorporate higher-order terms. Here, we have instead used the simple approximations stated for the normals and for the curvature. Since these are accurate only if the length disparity between adjacent edges is small, we have taken measures to ensure this in our simulation (see below).

The interfacial tension induces a force $\mathbf{F}_p^\gamma$ on a point p, which is given by

$$\mathbf{F}_p^\gamma = \hat{\mathbf{l}}_p^+ - \hat{\mathbf{l}}_p^-, \tag{B6}$$

where $\hat{\mathbf{l}}_p^\pm = \mathbf{l}_p^\pm / |\mathbf{l}_p^\pm|$ are the unit tangents of the edges to either side of the point p, assuming consistent orientation of consecutive edges (see Fig. 15). Since the Laplace law [Eq. (2)] requires the surface tension force to be normal to the inter-

face, we use this to define a normal to a point p as

$$\hat{\mathbf{n}} = (\hat{\mathbf{l}}_p^+ - \hat{\mathbf{l}}_p^-)/|\hat{\mathbf{l}}_p^+ - \hat{\mathbf{l}}_p^-|. \tag{B7}$$

Velocities and displacements

The velocity of a point p on a film is determined from the local geometry and the pressures of adjacent cells, according to the dimensionless viscous froth equation of motion,

$$v[\Delta P, K] = \Delta P - K. \tag{B8}$$

The velocity v is in the normal direction, its sign being chosen consistently with the signs of the pressure drop ΔP and curvature K. In the next time step δt, the resulting displacement is then made in the normal direction associated with this point. Once each point of the discretization has been displaced, we move all vertices in order to maintain angles of 120 degrees, using an (analytic) solution of the Fermat-Steiner problem [30]. This rule for vertex motion, albeit in the spirit of the arguments given in Sec. II D, is only correct to lowest order, since no curvature of the line segments is considered when determining their point of intersection. A more careful extrapolation procedure would be desirable, and is envisaged in future work. The error made by imposing 120 degree angles decreases as the discretization becomes finer, and can in principle be made arbitrarily small by successive refinements.

On the technical side, it is preferable to work with a tesselation of edges of comparable length, for which our discretization is most accurate. In order to achieve this, we define a narrow range for the desired edge length. After each time step, longer edges are refined and shorter ones fused. In our *ab initio* implementation, we have furthermore introduced small artificial tangential displacements of the discretization points, designed to keep the latter equally spaced while leaving the shape of the interface unchanged.

Bubble pressures and constant areas

After evaluation of the local geometry and calculation of the resulting surface tension forces, we must calculate the bubble pressures. In the general case [arbitrary exponent ν in the dissipation law, Eq. (7)] this can be done using an iterative procedure, introducing a penalty function to keep the bubble areas fixed. We will illustrate here a simplification, leading to a more efficient scheme, for the special case of a linear dissipation relation ($\nu = 1$). Any change in cell pressures leads to corresponding changes in the cell areas, and in this case the relationship is linear. The changes in cell areas are also subject to the generalized von Neumann's law [Eq. (10)], and hence are known independently. The existence of the generalized von Neumann law thus reduces the problem to a single solution of linear equations.

To this end, we integrate the equation of motion [Eq. (1)] around the boundary ∂b of an arbitrary bubble b. The change in area of the bubble is equal to the integral of the normal velocity field v on the surrounding films,

$$\frac{dA_b}{dt} = \oint_{\partial b} v \, dl = \oint_{\partial b} (\Delta P - K) dl. \tag{B9}$$

As in the derivation for the coarsening dynamics (see, e.g., [1,2]), Gauss' theorem says that the curvature must integrate around a bubble to 2π, deducting $\pi/3$ at each of the n_b vertices,

$$\frac{dA_b}{dt} = \frac{\pi}{3}(n_b - 6) + \sum_{b'} (P_b - P_{b'}) l_{bb'}, \tag{B10}$$

where the summation is over all bubbles b' adjacent to b, and where $l_{bb'}$ is the length of the film shared by bubbles b and b'. Generalizing the definition of a length $l_{bb'}$ to

$$l_{bb'} = 0 \quad \text{if } b, \ b' \text{ are not neighbors, or if } b = b', \tag{B11}$$

it becomes clear that the previous equation represents in fact a simple matrix equation for the N bubble pressures,

$$L_{bb'} P_{b'} = \dot{\alpha}_b, \tag{B12}$$

in which the vector P_b contains the bubble pressures. The matrix $L_{bb'}$ is a purely geometrical object, obtained by explicit summation for a given configuration,

$$L_{bb'} = \begin{cases} \sum_{b''} l_{bb''} = l_b^{\text{tot}} & \text{if } b = b' \\ -l_{bb'} & \text{otherwise} \end{cases}. \tag{B13}$$

l_b^{tot} is the total length of the perimeter of bubble b. Thus to find $L_{bb'}$ we need only to calculate the length of each film. The $N \times N$ matrix $L_{bb'}$ is sparse in a large bubble cluster, since its off-diagonal entries are nonzero only if bubbles b and b' share a film.

The calculation of the right-hand-side vector $\dot{\alpha}_b$ is also straightforward, although the nature of the calculation depends upon the situation. Its bth entry is

$$\dot{\alpha}_b = \frac{dA_b}{dt} - \frac{\pi}{3}(n_b - 6), \tag{B14}$$

where n_b is the number of sides of the bubble b. In the study of rheology, it is usual that the bubble areas do not vary, $dA_b/dt = 0$, leading to a further simplification. Nevertheless, gas diffusion is conceptually straightforward to include, since the area variation of a given bubble can be deduced from the generalized von Neumann law [Eq. (10)] for any given permeability constant κ.

The evolution of the network can now be projected a time step δt ahead, according to Eq. (B8). Two technical points are worthy of mention. (i) Even in the case of fixed bubble areas, slight numerical inaccuracies can lead to variations in the individual cell areas; we then choose a value of dA_b/dt for each bubble that restores its specified area. (ii) When applied to a periodic cluster, the matrix equation [Eq. (B12)] is singular. The eigenvector with zero eigenvalue corresponds to adding an overall constant to all cell pressures. It is therefore sufficient to determine *any* solution for the pressure, which can be done using special techniques [31].

[1] J.A. Glazier and D. Weaire, J. Phys.: Condens. Matter **4**, 1867 (1992).

[2] D. Weaire and S. McMurry, Solid State Phys. **50**, 1 (1997).

[3] A. Kabla and G. Debregeas, Phys. Rev. Lett. **90**, 258303 (2003).

[4] I. Cantat and R. Delannay, Phys. Rev. E **67**, 031501 (2003).

[5] A.M. Kraynik, Annu. Rev. Fluid Mech. **20**, 325 (1988).

[6] R.L. Fullman, in *Metal Interfaces* (American Society of Metals, Cleveland, 1952), p. 179.

[7] K. Kawasaki, T. Nagai, and K. Nakashima, Philos. Mag. B **60**, 399 (1989).

[8] T. Okuzono and K. Kawasaki, Phys. Rev. E **51**, 1246 (1995).

[9] D.J. Durian, Phys. Rev. Lett. **75**, 4780 (1995).

[10] I. Cantat, R. Delannay, and N. Kern, Europhys. Lett. **65**, 726 (2004).

[11] D. Weaire and S. Hutzler, *The Physics of Foams* (Clarendon Press, Oxford, 1999).

[12] J. von Neumann, in *Metal Interfaces* (American Society of Metals, Cleveland, 1952), p. 108.

[13] W.W. Mullins, J. Appl. Phys. **27**, 900 (1956).

[14] K. Brakke, *The Motion of a Surface by its Mean Curvature* (Princeton University Press, Princeton, NJ, 1978).

[15] C.S. Smith, in *Metal Interfaces* (American Society for Metals, Cleveland, 1952), p. 65.

[16] S.J. Cox, M.F. Vaz, and D. Weaire, Eur. Phys. J. E **11**, 29 (2003).

[17] D. Weaire and J.P. Kermode, Philos. Mag. B **47**, L29 (1983).

[18] D. Weaire and J.P. Kermode, Philos. Mag. B **48**, 245 (1983).

[19] J.P. Kermode and D. Weaire, Comput. Phys. Commun. **60**, 75 (1990).

[20] H. Aref and T. Herdtle, in *Topological Fluid Mechanics*, edited by H. Moffat and A. Tsinober (Cambridge University Press, Cambridge, U.K., 1990), p. 745.

[21] F.P. Bretherton, J. Fluid Mech. **10**, 16 (1961).

[22] C. Monnereau, B. Prunet-Foch, and M. Vignes-Adler, Phys. Rev. E **63**, 061402 (2001).

[23] D. Weaire, Philos. Mag. Lett. **68**, 93 (1993).

[24] H.J. Frost, C.V. Thompson, C.L. Howe, and J. Whang, Scr. Metall. **22**, 65 (1988).

[25] K. Brakke, Exp. Math. **1**, 141 (1992).

[26] D. Weaire, S. Hutzler, S. Cox, N. Kern, M.D. Alonso, and W. Drenckhan, J. Phys.: Condens. Matter **15**, S65 (2003).

[27] W. Drenckhan, Ph.D. thesis, Physics Department, Trinity College Dublin (2004).

[28] W. Drenckhan, F. Elias, S. Hutzler, D. Weaire, E. Janiaud, and J.-C. Bacri, J. Appl. Phys. **93**, 10 078 (2003).

[29] D.A. Reinelt and A.M. Kraynik, J. Colloid Interface Sci. **132**, 491 (1989).

[30] T. Green, L. Lue, and P. Grassia (unpublished).

[31] W.H. Press, S.A. Teukolsky, W.T. Vetterling, and B.P. Flannery, *Numerical Recipes in C* (Cambridge University Press, Cambridge, U.K., 1992).